JOURNAL OF COMPUTATIONAL PHYSICS 43, 268–288 (1981)

Magnetohydrodynamic Particle Code: Lax–Wendroff Algorithm with Finer Grid Interpolations

F. BRUNEL, J. N. LEBOEUF, T. TAJIMA, AND J. M. DAWSON

Department of Physics, University of California, Los Angeles, California 90024

M. MAKINO

Department of Electrical Engineering, Nagoya University, Nagoya, Japan 464

AND

T. KAMIMURA

Institute of Plasma Physics, Nagoya University, Nagoya, Japan 464

Received September 19, 1980; revised July 7, 1981

Two marked improvements of algorithms for the magnetohydrodynamic particle code which treats elements of the fluid as finite-size particles are reported. First a Lax–Wendroff algorithm is introduced in the magnetic field pusher making the code nearly dissipationless. Second, a number of improvements to the sharpness of the mode spectra, reduction of noise, dispersion, numerical heating of fluid elements, and improved stability have been achieved by various choices of the methods for assignment of particle quantities to grid points and interpolation of grid quantities at the particle positions. Properties of the various versions of the code have been studied and compared. Applications to the ballooning mode instability, to the endloss problem of a high-beta plasma column with sharp boundaries, and to global MHD simulations of the magnetosphere are presented.

I. INTRODUCTION

A particle method of solving the plasma equations on the level of hydrodynamics [1, 2] and magnetohydrodynamics (MHD) has been introduced and extensively developed in previous work [3]. It treats elements of the fluids as finite-size particles. It solves exactly for the orbits of the particles much as is done in conventional particle codes; here MHD forces are employed in the place of the conventional Lorentz force. The MHD forces result from a certain coarse-graining of time scales involved in the plasma physics process: if it is ideal MHD, the simulation "particles" represent a fluid ensemble of ions and electrons and become charge neutral, carrying

0021-9991/81/100268–21$02.00/0

only mass but no charge. It is possible to generalize the codes by adding, for example, finite resistivity effects as done in Ref. [4] or the Hall term as done in Ref. [5]. Addition of these terms sometimes changes the ordering of the time scales involved and may require careful considerations of the algorithm. A fixed background grid is introduced upon which the magnetic field is defined and the fluid quantities such as velocity and density are accumulated from the particle velocities and positions, as is done for the charge density and currents in a conventional particle code. The particle quantities are then pushed in a Lagrangian way while the field quantities are advanced in an Eulerian manner. Computational burdens are, so to speak, split into two different levels: the sub-grid level (particles) and the grid level to facilitate the description of MHD activities. Because of its particle nature (the Lagrangian part of the code), this algorithm naturally handles convection and exactly conserves mass and momentum. In conventional Eulerian codes, on the other hand, because of the advective derivatives in the fluid equations, the density could go negative, for example, and unphysical instability result unless special cures are introduced to supress this as in the flux conservative transport (FCT) [6]. The introduction of a fixed background grid (the Eulerian part of the code) circumvents grid entanglement resulting from complicated fluid motion inherent to conventional Lagrangian fluid codes. The use of particles to describe the fluids has some disadvantages: (i) significant increase of memory for particle quantities and of time required to handle particle computation, (ii) some noise problem absent in conventional fluid codes but not as excessive as in the charged particle codes. However, the general physical nature of the codes, their simplicity and ability to yield physical results with a minimum of ad hoc assumptions and the ease with which they can be modified to include additional physical effects make this class of code very useful. In this paper we report two substantial improvements to the work [3]. Previously [3], to assign fluid quantities onto the mesh from particle quantities and, inversely, to assign the force on particles from the mesh quantities, a coarse interpolation, the nearest grid point method (NGP), was employed. Although sufficiently large grid and numbers of particles can alleviate numerical coarseness, speed and economy require an improvement on this. To update the magnetic field, we employed the Lax method [7] in Ref. [3]. Although the algorithm is simple and stable, it gives rise to numerical diffusion of magnetic fields for problems where plasma quantities vary rapidly in space. Therefore, improvement is desired here as well. For the first improvement, we have tested several grid-particle assignment (interpolation) techniques and compared them to each other; here we report on the area weighting method and the subtracted dipole (SUD) method [8]. For the second, we have examined several varieties of the time-centered Lax–Wendroff method [7] to reduce the numerical diffusion of the previous Lax method. Actual implementation of the Lax–Wendroff algorithm couples to the particle grid assignment to a certain extent. It is known [9] that the conventional Eulerian Lax–Wendroff algorithm is nonlinearly unstable (explosive instability) to odd–even grid fluctuations even though it is linearly stable. This phenomenon is in general controlled by introducing numerical diffusion terms in the equations such as the continuity equation and the equation of motion, or by resorting to the FCT

method [6, 9], where the stabilizing numerical diffusion terms are offset by the so-called anti-diffusion terms. In the present MHD particle code, however, the Lax–Wendroff algorithm is stable to these types of perturbations with no recourse to added numerical diffusive terms being required.

We discuss the Lax–Wendroff scheme and its actual implementation with various interpolation schemes in Section II. We also make a comparison of the Lax–Wendroff code with the Lax method in this section. A code version which handles all the derivatives in Fourier space with the SUD assignment is detailed in Section III, while another version of the code which treats derivatives by finite differences, with an area weighting assignment is reported in Section IV. Applications of the present codes are given in Section V and a discussion presented and conclusions drawn in the final section.

II. Lax–Wendroff Scheme

(A) *Algorithm*

In the MHD regime the magnetic induction equation (Faraday's law) cannot be cast, in a straightforward manner, in a time-centered finite difference form. In order to make it virtually time centered, the magnetic induction equation

$$\frac{\partial}{\partial t}\mathbf{B} = \nabla \times (\mathbf{v}_f \times \mathbf{B}) \tag{1}$$

is pushed using the Lax–Wendroff method [7, 10] as follows; a first approximate step is taken

$$\mathbf{B}^{n+1/2} = \langle \mathbf{B}^n \rangle + [\nabla \times (\mathbf{v}_f^n \times \mathbf{B}^n)] \frac{\Delta t}{2}, \tag{2}$$

followed by

$$\mathbf{B}^{n+1} = \mathbf{B}^n + [\nabla \times (\mathbf{v}_f^{n+1/2} \times \mathbf{B}^{n+1/2})] \Delta t, \tag{3}$$

where $\mathbf{v}_f$ stands for the fluid velocity and superscripts refer to the time step. The angular bracket denotes averaging over the neighboring spatial cells, i.e.,

$$\langle \mathbf{B} \rangle_{ij} = (\mathbf{B}_{i+1,j} + \mathbf{B}_{i-1,j} + \mathbf{B}_{i,j+1} + \mathbf{B}_{i,j-1})/4$$

at grid (i, j) for a two dimensional case, subscripts representing the mesh points. On the other hand, the particle quantities are advanced in time using the following leap-frog scheme

$$\mathbf{v}_i^{n+1/2} = \mathbf{v}_i^{n-1/2} + \frac{1}{\rho}[-\nabla p + (\nabla \times \mathbf{B}) \times \mathbf{B}/4\pi]_i^n \Delta t, \tag{4}$$

$$\mathbf{x}_i^{n+1} = \mathbf{x}_i^n + \mathbf{v}_i^{n+1/2} \Delta t, \tag{5}$$

where ρ and p are the plasma density and pressure defined on grid points which are interpolated at the position of the ith particle. The details of this interpolation are discussed in later sections. The derivatives are evaluated either by means of finite diferences or by Fourier transformation techniques. The full scheme for the code is detailed in Table I.

The two step Lax–Wendroff method is a nearly dissipationless time-centered method, accurate to the second order in $k\Delta$ where Δ is the mesh size and k is a typical wavenumber. The first step (Lax step) of the scheme, Eq. (2), is only used for the sake of facilitating the calculation of the magnetic field at centered time on the right-hand side of Eq. (3), the second step. By so doing, Eq. (3) now becomes time

TABLE I

Lax–Wendroff Scheme for an MHD Particle Code

Initially we have: $\mathbf{B}^n$, $\mathbf{x}^n$, $\mathbf{v}^{n-1/2}$.

(1) Compute fluid density: $\rho^n = fct(x^n)$

(2) Compute magnetic and fluid forces:

$$\mathbf{F}_B^n = (\nabla \times \mathbf{B}^n) \times \mathbf{B}^n / 4\pi\rho^n$$

$$\mathbf{F}_p^n = -\nabla p^n / \rho^n, \quad \text{where} \quad p = fct(\rho)$$

(3) Push velocities half a time step:

$$\mathbf{v}^n = \mathbf{v}^{n-1/2} + \mathbf{F}^n \Delta t/2,$$

where $\mathbf{F}^n = \mathbf{F}_p^n + \mathbf{F}_B^n$

(4) Compute fluid velocities: $\mathbf{v}_f^n = fct(\mathbf{v}^n, \mathbf{x}^n)$

(5) Push $\mathbf{B}$ half time step using Lax:

$$\mathbf{B}^{n+1/2} = \langle B \rangle^n + (\nabla \times (\mathbf{v}_f^n \times \mathbf{B}^n))\, \Delta t/2,$$

where $\langle \mathbf{B} \rangle_{i,j}^n = (\mathbf{B}_{i+1,j}^n + \mathbf{B}_{i-1,j}^n + \mathbf{B}_{i,j+1}^n + \mathbf{B}_{i,j-1}^n)/4$

(6) Push velocities half a time step

$$\mathbf{v}^{n+1/2} = \mathbf{v}^n + \mathbf{F}^n \Delta t/2 + f(\mathbf{v}_f^n - \mathbf{v}^n)$$

where f is an optional drag term $0 \leqslant f \leqslant 1$ which removes multi-streaming (if $f = 1$)

(7) Push positions half a time step:

$$\mathbf{x}^{n+1/2} = \mathbf{x}^n + \mathbf{v}^{n+1/2} \Delta t/2$$

(8) Compute fluid velocities: $\mathbf{v}_f^{n+1/2} = fct(\mathbf{v}^{n+1/2}, \mathbf{x}^{n+1/2})$

(9) Push $\mathbf{B}$ with a full step:

$$\mathbf{B}^{n+1} = \mathbf{B}^n + \nabla \times (\mathbf{v}_f^{n+1/2} \times \mathbf{B}^{n+1/2}))\, \Delta t$$

(10) Push position half a time step: $\mathbf{x}^{n+1} = \mathbf{x}^{n+1/2} + \mathbf{v}^{n+1/2} \Delta t/2$

centered. For particle pushing, only these time-centered magnetic fields are employed in Eq. (4), thus minimizing the diffusion inherent in the Lax step. By doing a signal analysis and considering a constant velocity as in Potter [7], one finds a norm for the amplification matrix which is given by

$$|g|^2 = 1 + 4k^4 \Delta^4 \alpha \left(\alpha - \frac{1}{N}\right), \tag{6}$$

where $\alpha = (v\Delta t/2\Delta)^2$ and N is the number of spatial dimensions. A Von Neumann stability criterion is obtained from Eq. (6) as

$$\Delta t \lesssim \sqrt{2}\Delta/c$$

for a two dimensional plasma with c being the fastest velocity of the system.

(B) *Interpolation Scheme and Dispersion Relation*

The dispersion relation of the modes is highly dependent on the interpolation scheme used, especially for large values of the wavenumber k. In this subsection, finite grid size effects in the MHD particle code are studied and dispersion relations for the sound and Alfven waves are obtained; these will be compared later on with values obtained from numerical experiments.

The force acting on a particle at $x = x_\alpha$ is affected by the force field at the various grid points; a weighted sum of these must be taken into account for the fact that the particle is not located at a grid point and it has finite size [11]. For simplicity let us assume a functional variation in the x direction only. Then the force acting on the particles is expressed [12] as

$$\mathbf{F}(x_\alpha) = \int dx\, f(x_\alpha - x) \sum_i w(x - x_i)\, \mathbf{F}_i, \tag{8}$$

where the subscript α stands for the αth particle, f is the form factor of the particle and w is a weighting factor arising from the interpolation to the particle position of a grid quantity force whose linearized expression is

$$\mathbf{F}_i = -\frac{c_s^2}{n_0} \nabla n_i + \frac{1}{4\pi\rho_0} (\nabla \times \mathbf{B}_i) \times \mathbf{B}_0, \tag{9}$$

with the grid quantities n_i and $\mathbf{B}_i$ being the density and magnetic field perturbation. In k-space, Eqs. (8) and (9) become

$$\mathbf{F}(k) = S(k)\left[-\frac{c_s^2}{n_0} i\boldsymbol{\kappa} n(k) \right] + \frac{1}{4\pi\rho_0} i[\boldsymbol{\kappa} \times \mathbf{B}(k)] \times \mathbf{B}_0$$

and

$$S(k) = f(k)\, w(k), \tag{10}$$

and the term $\boldsymbol{\kappa}(k)$ represents the spatial derivative and is in the x-direction.

The density perturbation is evaluated by considering the particle orbits described by straight lines with small deflections due to the force term. The perturbation of the distribution function is given by

$$f_1 = -\mathbf{v}_\alpha \cdot \frac{\partial f_0}{\partial \mathbf{v}} = -i \frac{\mathbf{F}(k)}{\omega - k v_x} \cdot \frac{\partial f_0}{\partial \mathbf{v}}, \tag{11}$$

with $\mathbf{v}_\alpha$ being the velocity perturbation due to the force $F(k)$. This system is indeed described by a Vlasov equation for one species of particles with a force term given by Eq. (9) [12]. The MHD aspects are, however, retrieved when we consider the moments of that equation. If one really wants to represent a system described by MHD equations, multi-streaming should be avoided by some means such as a relative drag between particles with different velocities in the same cell [2], as shown in Table I, Item (6). The density perturbation is then

$$n(k) = i \frac{n_0}{\omega} \sum_{p=-\infty}^{\infty} S(k_p)\, \mathbf{F}(k_p) \cdot \boldsymbol{\psi}(k_p, \omega), \tag{12}$$

where

$$\boldsymbol{\psi}(k, \omega) = -\frac{1}{n_0} \int \frac{d^3 v}{1 - \dfrac{k v_x}{\omega}} \frac{\partial f_0}{\partial \mathbf{v}} \tag{13}$$

and

$$k_p = k + 2\pi p,$$

with p being an integer. The terms with $p \neq 0$ in the summation represent the spatial aliases.

The set of equations is closed by including Eq. (1); they then become

$$-i\omega \mathbf{B} = i\boldsymbol{\kappa} \times (\mathbf{v}_f \times \mathbf{B}_0),$$

with

$$\mathbf{v}_f = i \frac{\mathbf{F}(k)}{\omega} \sum_{p=-\infty}^{\infty} S(k_p)\, \psi_v(k_p),$$

$$\psi_v(k) = \frac{1}{n_0} \int d^3 v \frac{\mathbf{v}}{1 - \dfrac{k v_x}{\omega}} \cdot \frac{\partial f_0}{\partial \mathbf{v}}. \tag{14}$$

Let us consider a homogeneous magnetic field B_0 parallel to the x axis and consider the sound waves (longitudinal velocity perturbation) and Alfven waves propagating

along this axis. The dispersion relation obtained for the sound wave is the following

$$\omega^2 = S^2(k)\,\kappa(k)\,kc_s^2\left(1 + 3\frac{v_T^2}{c_s^2}\right), \tag{15}$$

while that for the Alfven wave is

$$\omega^2 = c_A^2\,S^2(k)\,\kappa^2(k). \tag{16}$$

Here we have kept only the fundamental and have neglected all the aliases. The thermal speed v_T of the "particle" velocity distribution $f_0(v)$ is assumed much smaller than c_s and c_A.

(C) *Comparison between the Lax and the Lax–Wendroff Method*

The Lax scheme and the Lax–Wendroff scheme are compared on the basis of mode spectra from the NGP versions. The dispersion relations of the sound wave and Alfven wave have been measured from thermal runs on two-and-one-half dimensional (two space and three velocity dimensions) codes. Time auto-correlations of the magnetic field and density fluctuations have been taken and frequency spectra derived from them. The parameters for the runs are: the Alfven speed $c_A = 4c_s$, the grid size 32×32 with four particles per cell. The runs extend to 2000 time steps ($t = 200\Delta/c_s$). The results for both dispersion relations have been plotted in Figs. 1a, b and compared to the theoretical results predicted by Eqs. (15) and (16) (we take k parallel to the x-axis). For the sound wave we use gaussian shaped particles, thus $f(k) = \exp(-k^2a^2/2)$ with $a = \Delta$, and we evaluate the pressure gradient using fast Fourier transforms, i.e., $\kappa(k) = k$. For the magnetic term we have no form factor, i.e., $f = 1$, and we use finite differences to evaluate the magnetic pressure gradient so that $\kappa(k) = k(\sin k\Delta/k\Delta)$. NGP weighting yields $w(k) = \sin(k\Delta/2)/(k\Delta/2)$. Equations (15) and (16) become respectively

$$\omega^2 = \exp(-k^2a^2)\left(\frac{\sin(k\Delta/2)}{k\Delta/2}\right)^2 k^2c_s^2, \tag{17}$$

and

$$\omega^2 = \left(\frac{\sin k\Delta}{k\Delta}\right)^2\left(\frac{\sin k\Delta/2}{k\Delta/2}\right)^2 k^2c_A^2. \tag{18}$$

Fair agreement with the theory (Eq. (18)) is obtained for the Alfven wave with the Lax method (Fig. 1a). It is slightly better with the Lax–Wendroff method (Fig. 1b). While this is not apparent from Figs. 1a, b, the frequency spectra are observed to be both cleaner in the Lax–Wendroff case than in the Lax one (i.e., the spectral peaks at the characteristic frequencies appear prominently, an indication of lower numerical noise) and sharper (i.e., their full width at half maximum is narrower, a reflection of the nearly dissipationless character of the algorithm.) For the sound wave, the correlation points of Figs. 1a, b lie above the theoretical curve predicted by Eq. (17).

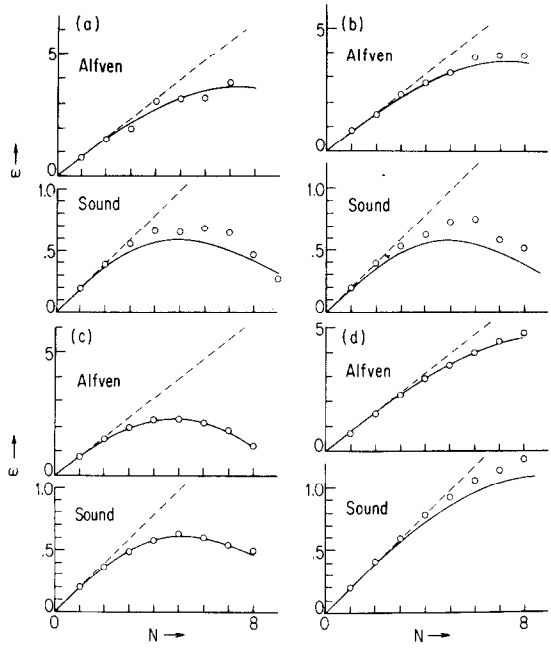

FIG. 1. Dispersion relation of Alfven and sound waves for (a) Lax NGP version of this code, (b) Lax–Wendroff NGP, (c) Lax–Wendroff Fourier SUD, and (d) Lax–Wendroff area sharing; we used $k = 2\pi N/32$.

The reason for this discrepancy is the contribution made by the random thermal particle motion as shown by Eq. (15). However, even if we start with a negligible thermal velocity $v_T = 0.1c_s$, at the end of the run the thermal velocity becomes $v_T = 0.4c_s$ due to the numerical heating associated with aliases at large k. This heating makes the simulation points fall higher than the theoretical prediction for the large wavenumbers. Since correlation diagonistics are essentially time averaged ones and the heating is time dependent, it is difficult to define a numerical v_T^2 to better fit Eq. (15) to the simulation frequencies. The numerical noise and heating of the "particles" (fluid elements) can be reduced and both Alfven and sound wave dispersion relations become closer to theory by adopting more elaborate algorithms as described in the following sections.

III. Fourier Space Algorithm with the Subtracted Dipole Interpolation

The Lax–Wendroff scheme was implemented using several different versions in order to experimentally determine an optimal choice of algorithm, although in these studies we were guided by existing theoretical considerations and experience. The different versions tested differ primarily in the way the particle and grid quantities are

related: NGP, SUD, area weighting, etc., were used. Another aspect which was varied was the method of calculating spatial quantities from grid quantities: Fourier space handling using the fast Fourier transform (FFT) and finite differences were used. Since conventional particle codes at the University of California at Los Angeles employ SUD for calculating the field quantities in Fourier space, one natural improvement over the original Lax code with NGP [3] is to apply the same algorithm, i.e., the SUD algorithm for calculating the grid quantities in Fourier space for the Lax–Wendroff particle MHD code. In this section we describe this approach. In the next section we present an alternative approach via finite differences in real space with area weighting interpolation.

All the force terms (the particle pressure and magnetic force) are calculated as spatial derivatives of the stress tensors (pressure and Maxwell's stress tensor) in Fourier space. Each particle is assigned a Gaussian–shaped mass distribution with a Gaussian form factor interpolated by the SUD method [11, 13]. The interpolation function for SUD in Fourier space is

$$w(k) = \frac{2}{k\Delta} \sin^3 \frac{k\Delta}{2} + \frac{4}{k^2\Delta^2} \sin^2 \frac{k\Delta}{2} \cos \frac{k\Delta}{2}. \tag{19}$$

Equation (19) is approximately unity for $k\Delta \lesssim \pi/2$; hereafter we neglect its deviation from unity. The expressions of the dispersion relations for sound and Alfven waves obtained from Eqs. (15) and (16) are

$$\omega^2 = e^{-k^2a^2} k^2 c_s^2, \tag{20}$$

$$\omega^2 = e^{-k^2a^2} \left(\frac{\sin k\Delta}{k\Delta} \right) k^2 c_A^2. \tag{21}$$

Time correlations of the density and magnetic field for the various k modes have been taken for runs with the same parameters as in Section II (C). Good agreement is observed with Eqs. (20) and (21) for the sound wave and the Alfven wave as shown in Fig. 1c. Numerical heating of the particles does not occur now and the thermal energy of particles does not increase for $a = 1\Delta$, a great improvement over the NPG version. Another improvement, not apparent from Fig. 1c, is that the near absence of numerical noise and particle heating makes the frequency spectra cleaner and sharper at the large k than those from the NGP scheme.

The dispersion of the waves due to the finite size of particles becomes significant for large wavenumbers, i.e., $n \geqslant 5$ with $k = 2\pi n/L$ and $L = 32\Delta$ (see Fig. 1c). These modes with significant dispersion, however, heavily damp and do not contribute to the transport to a large extent. If a substantially smaller particle size ($a \lesssim 0.7\Delta$) is used, the code is unstable to numerical heating of the particles. A reasonable explanation is that a reduced particle size gives less suppression of the high k modes allowing greater effects of aliasing to produce numerical heating of the particles.

IV. Finite Difference Algorithm with the Area Weighting Interpolation

A finite difference algorithm for the Lax–Wendroff scheme using area weighting interpolation [1] has been implemented in parallel to the Fourier transform algorithm with dipole interpolation (Section III). It can be shown for charged particle codes [13] that the area weighting scheme is equivalent to the dipole interpolation one and that both are accurate to the second order in $k\Delta$. In addition, implementation of complicated boundary conditions is generally easier and extension to a curvilinear coordinate system more straightforward for the finite difference scheme. It is, therefore, worthwhile to examine the properties of both types of algorithms and compare one to other for the case of the MHD particle code.

The version presented here employs an area weighting algorithm for the computation of the density and the fluid velocity from particles as well as for assigning the force on the particles. In order to increase the stability and to keep the particle heating negligible, a particle size (area weighting distance) of typically $1 \leqslant a \leqslant 2$ is used. The contribution to the density due to one particle at one grid point is proportional to the area of the particle overlapping the grid point; the same principle is used to evaluate the share of the force coming from one particular grid point to the particle position for pushing the particle. In one dimension, for example, the force sharing may be written as

$$F_\alpha = w_{i-1}F_{i-1} + w_iF_i + w_{i+1}F_{i+1}$$

with

$$\begin{aligned} w_{i-1} &= \max\{(a-1)/2 - dx, 0\}/a, \\ w_i &= \min\{(a+1)/2 - |dx|, 1\}/a, \\ w_{i+1} &= \max\{(a-1)/2 + dx, 0\}/a, \end{aligned} \tag{22}$$

where the point i is the nearest grid at a distance $(-dx)$ from the particle. Such force sharing, Eq. (22), yields a weighting function in Fourier space which is

$$w(k) = \left(\frac{\sin ka/2}{ka/2}\right)\left(\frac{\sin k\Delta/2}{k\Delta/2}\right). \tag{23}$$

It turns out to be necessary in this version to introduce a double staggered mesh system in order to keep the grid noise and particle heating as low as in the Fourier transform algorithm with dipole interpolation version of the particle MHD code. A single grid suffices in charged particle codes to achieve this. In the MHD particle code shorter range forces come into play. The short wavelengths or large wavenumbers are more emphasized (the pressure force, for instance, goes like kp while the electrostatic force goes like ρ/k in 1D) and a finer treatment of the difference operations is required; hence the staggered grid. When we use a single grid as in Section III, we observe a substantial increase in the particle random motion

(kinetic energy of the particles) larger than that of the Lax and NGP version with a Gaussian form factor. Also, the wave spectra for he sound waves are neither clear nor sharp.

A second staggered grid is introduced at the half position and the grid quantities from the full position mesh is transferred to the half position mesh when one is evaluating the spatial derivatives which, for example in the case with respect to x, is expressed as

$$\left(\frac{\partial A}{\partial x}\right)_{i+1/2,j+1/2} = \frac{1}{2}(A_{i+1,j} - A_{i,j} + A_{i+1,j+1} - A_{i,j+1}). \tag{24}$$

The density and fluid velocity can be either accumulated on the full or half position mesh. Consider Table I for the Lax–Wendroff scheme. When the single grid system takes every operation on a single grid, the double grid system alternates the grid as follows. The particle velocity and magnetic field, at the full time step n are still defined on the integral position mesh, while the force pushing the particle and the intermediary value for the magnetic field are defined on the half position mesh. With this double mesh, the sound wave spectrum is much improved and the heating rate is reduced at least by a factor of two.

Time autocorrelations of the density and the magnetic field for different k's have been taken for parameters identical to Section II(C) but with a particle size $a = 1.4\Delta$. The dispersion relation has been plotted from the correlation data for the sound and Alfven waves (Fig. 1d) and compared with the theoretical curves described by Eqs. (15) and (16), respectively:

$$\omega^2 = \left(\frac{\sin ka/2}{ka/2}\right)^2 \left(\frac{\sin k\Delta/2}{k\Delta/2}\right)^3 k^2 c_s^2, \tag{25}$$

$$\omega^2 = \left(\frac{\sin ka/2}{ka/2}\right)^2 \left(\frac{\sin \Delta/2}{k\Delta/2}\right)^4 k^2 c_A^2, \tag{26}$$

Here we took $\kappa(k) = 2/\Delta \sin k\Delta/2$ because of our double grid system. The frequency spectra are as clean and as sharp as those obtained for the Fourier Transform algorithm with dipole interpolation and the simulation frequencies measured plotted in Fig. 1d. It shows closer agreement between theory and simulation than Fig. 1b obtained in II(C) with the NGP version of the code. The Alfven wave dispersion relation from the simulation is well described by Eq. (26). Because there is much less thermal noise, the sound waves dispersion relation is much closer to the theoretical curve than in the case of the NGP run. The particle random motion increases only by a small amount here. Starting with a thermal velocity $v_T = 0.1c_s$, we have $v_T = 0.2c_s$ after 2,000 time steps, which is a small increase in energy when we compare it with the average kinetic energy for a particle $c_s^2/2m$. However, the sound wave dispersion relation agrees better with theory for the Fourier Transform algorithm with dipole interpolation than for the two-grid area-weighting finite difference version.

Nevertheless, there is much less dispersion at the large k modes in the latter (Fig. 1d) than in the former (Fig. 1c) for both Alfven and sound waves because of the different form factors attached to the particles.

V. Applications

Some applications of these various versions of the Lax–Wendroff code to physics problems are given in this section: (a) the ballooning instability, (b) the problem of endflow from a high-beta plasma column, and (c) a global simulation of the

the Lax scheme. This is because numerical diffusion of the magnetic field through the plasma quickly creates a diffuse plasma-field boundary [7] thereby creating undesired pressure, density, field profiles which alter instability or other dynamic behavior we desire to model. For the third problem, although some global hydrodynamical aspects of the magnetosphere may be satisfactorily modeled by the Lax algorithm, one notable shortcoming in such simulations [15] has been a short magnetotail, since the high local numerical field diffusivity causes an immediate reconnection of magnetic field lines behind the dipole field for a southward configuration of the solar wind (directed opposite to the dipole). The implementation of the Lax–Wendroff scheme enable us to reduce the numerical diffusion in the magnetic field by a substantial amount. Note that the fluid equations are always integrated by the time-centered leap-frog scheme and do not cause excessive viscosity in either the Lax or the Lax–Wendroff codes. As we shall see in the following, the Lax–Wendroff scheme can handle the cases where the plasma is highly nonuniform.

(A) *Ballooning Instability*

The nonresistive MHD ballooning instability occurs in magnetic systems with good and bad magnetic field curvature; roughly speaking it is an interchange instability predominantly localized to the bad curvature regions. Its structure is such that perturbations vary not only perpendicular to the field lines ($k_\perp$) but also parallel to the field lines, i.e., $k_\parallel \neq 0$. We have made preliminary simulations of this instability using the simplest model which incorporates its essential features. The model is a slab of plasma perpendicular to the y axis. The magnetic field lines lie in the x–z plane and are tilted at a slight angle to the z-axis. The effects of good and bad curvature are mocked up by imposing a gravitational field of the form $\mathbf{g} = g_0(L_y/L_x) \cos 2\pi_x/L_x \sin 2\pi y/L_y \hat{e}_x + g_0 \sin 2\pi x/L_x \cos 2\pi y/L_y \hat{e}_y$. This form of gravitational field is chosen because it can be derived from a potential and hence the plasma motion is energy conserving. The tilt of the field lines in the x-direction means that stable and unstable regions are connected along field lines. In the simulation it is assumed that all quantities are independent of z ($2 - 1/2$D model). We have also used a model which is periodic in the y-direction for simplicity in solving for B; this also accounts for the forms chosen for g.

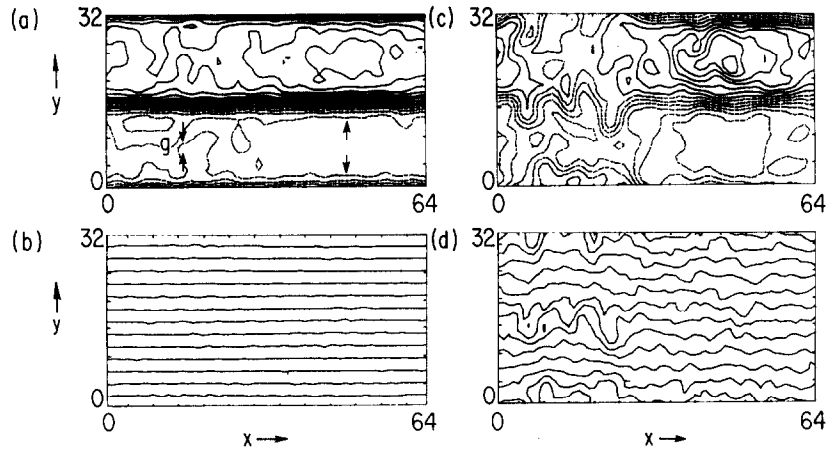

FIG. 2. Ballooning instability with the 2–1/2D code. (a) Density contours at $t = 10\Delta/c_s$ before the onset of the instability; the arrows inside labeled **g**, indicate the direction of the gravitational force in the stable regions as well as in the unstable one. (b) Projection of the magnetic field lines in the x–y plane at the same time ($t = 10\Delta/c_s$). (c) Density contours after the onset of the ballooning instability at $t = 60\Delta/c_s$. The magnetic field lines at the same time ($t = 60\Delta/c_s$).

Our simulation involved an x–y grid which was 64×32. The plasma slab was confined between $y = 16$ and $y = 32$. It has a sharp boundary with a plasma β of 0.06 and $g_0 = 0.1$. The tilt of the field lines was varied from $\theta = 0°$ to 5°. The results of a typical simulation for $\theta = 1°$ are shown in Fig. 2. Figures 2a, c show density contours at $t = 10\Delta/c_s$ and $60\Delta/c_s$; Figs. 2b, d show the projection of magnetic field lines on the x–y plane. The direction of g is shown in Fig. 2a. The plasma is unstable on the left and stable on the right. The ballooning is clearly visible in Figs. 2c, d. For large tilt angles, $\theta \gtrsim 5°$, we find the plasma is stable.

This can be understood from the following physical arguments. When the connection length between the good and bad curvature regions, $L_c = L_x/2 \sin \theta$, is short enough that an Alfven wave can travel between them in a time smaller than a few e-folding times of the mode, γ^{-1}, the mode can be stabilized by transmitting energy to being tied to the stable region; only the average g which is zero is important. This time should be $(L_c/2\pi c_a) = (L_x/4\pi c_a \sin \theta)$, where L_x is the wavelength between good and bad regions. The stability criterion may be written

$$L_c/c_A \lesssim 2\pi/\gamma. \tag{27}$$

Now $\gamma \cong \sqrt{gk_\perp}$ is the growth rate for the flute interchange mode with sharp boundary. However, because of the tilt of the field lines there is a stabilizing influence for large k_x associated with bending the field lines. Marginal stability is achieved when a mode with one wavelength in the bad region is just unstable. In our two dimensional case, however, the parallel wavelength is tied to the perpendicular wavelength, i.e., $\lambda_\perp = \lambda_\parallel$

sin θ. The stability criterion, Eq. (27), for a mode with the longest parallel wavelength $\lambda_\parallel/2 = L_c$ is therefore expressed as a function of $\lambda_\perp$ and θ:

$$\lambda_\perp/2c_A \sin\theta \lesssim 2\pi\lambda_\perp^{1/2}/(2\pi g)^{1/2}. \tag{28}$$

Equation (28) says that for a fixed $\lambda_\perp$ there is a minimum angle θ_c above which the system is stable against the ballooning instability. For the present parameters we obtain the critical angle from Eq. (28) $\theta_c \simeq 5°$. Thus the stability transition as well as the critical angle observed in our simulation fit very well with the simple estimate made from Eq. (28).

Some remarks are due here concerning the limitations of our present model. Because of the two dimensional restriction, $k_\parallel$ is related to $k_\perp$ by θ and the plasma is not free to minimize θ in order to find a more unstable mode. A proper treatment really calls for a three dimensional model.

In the unstable cases in our simulation, all the basic features of the ballooning modes (except for the $\lambda_\perp$ dependence of the stability due to the two dimensionality of the model) have been observed. First, the projection of the magnetic field lines in the x–y plane as shown in Fig. 2d follows closely the contours of equal density (Fig. 2c) as it must be for the case when there is no resistivity (nonresistive ballooning.) Second, in terms of ordering of the spatial derivatives of density and magnetic fields, we notice, as mentioned by Glasser [17], that the perpendicular wavelength along x is much shorter than the parallel one, since $k_\parallel/k_\perp = \tan\theta \ll 1$; also we have $\partial/\partial y \ll ik_\perp$ as can be seen by the shearing aspect of the field lines in Fig. 2d, which means that the bending and compressing terms in the energy principle [17], are minimized as they should be.

With the 3D version of the code, ballooning instabilities have been obtained. We use the same model as in 2D for the x–y cut but the external magnetic field remains purely in the z-direction. The gravitational field is still pointed in the y-direction, but is in the unfavorable direction in the region where the coordinate z is small, while in the large z region it becomes favorable. The z-direction has been stretched for the present run such that the unit grid length in the z-direction $\Delta z = 100\Delta x = 100\Delta y$ in order to allow a mode structure with $k_\parallel/k_\perp \ll 1$. With a system of $16 \times 16 \times 16$ grids we see ballooning instability in the unfavorable region (see Fig. 3) albeit its small scale, since the condition for instability $L_c/c_A \gtrsim 2\pi/\gamma$ is very well satisfied. It seems, thus, that the present code is able to reasonably describe the ballooning instability.

(B) *Column Outflow*

A plasma column is confined by a magnetic field parallel to the column (the θ-pinch or long solenoid configuration) in the normal direction to the field lines, while the plasma freely moves along the field lines and escapes at the open ends. We wish to understand the influence of finite β on the confinement (generation of a self mirror) and the outflow of a high beta plasma column with sharp boundaries; an isotropic pressure is used. The outflow is modeled by removing the particles that touch the end of the column. The field boundary condition is periodic. The code naturally handles

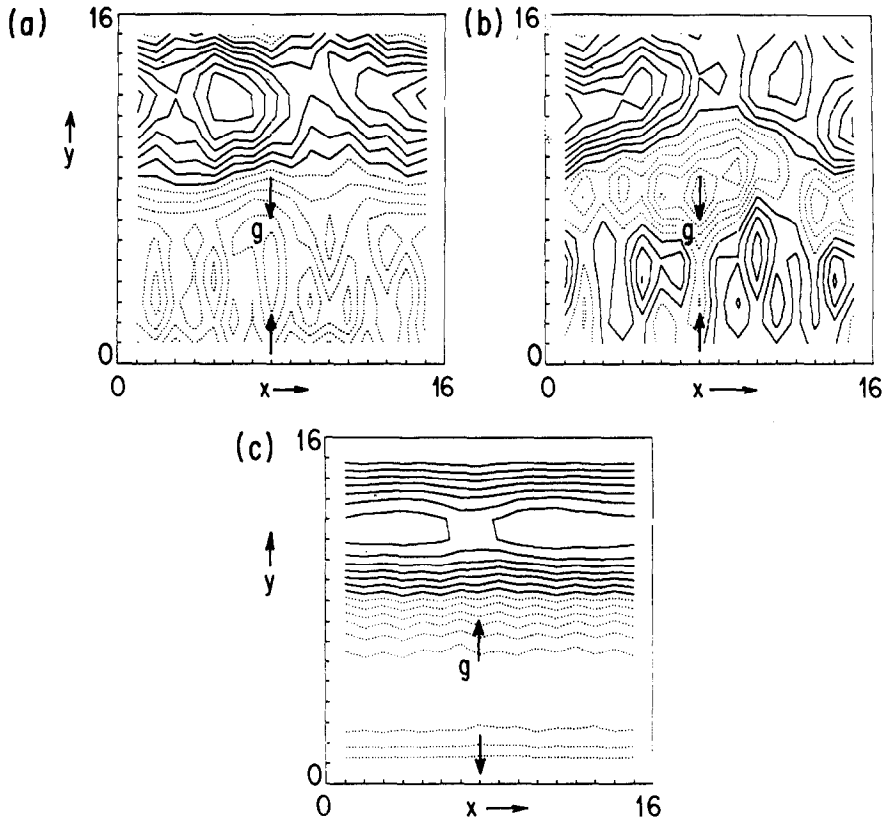

FIG. 3. Ballooning instability in 3D; (a) density contours in the unstable region before the onset of the instability at $t = 40\Delta/c_s$, (b) density contours in the same region after the onset of the instability at $t = 60\Delta/c_s$, (c) density contours in the stable region at the same time, i.e., $t = 60\Delta/c_s$.

the sharp density gradient due to its particle nature and the low resistive diffusion of the Lax–Wendroff scheme. A drag term ν defined as in Ref. [1] is used to suppress multistreaming ($\nu = 1$). With a system size $128\Delta \times 64\Delta$ we start with a high density column of 20 particles per cell with a diameter of 16Δ, the region outside the column is filled with a low density plasma of four particles per cell to keep the Alfven velocity finite [18]. A strong magnetic field in the x-direction is applied outside a weaker one inside the column so that perpendicular pressure balance is satisfied.

In the previous theories for a sharp boundary plasma, an infinite confinement time is predicted at $\beta = 1$ [19], since an infinitely large self mirror is produced (here β is the ratio of the plasma pressure in the column to the magnetic pressure outside.) This theory gives an outflow proportional to the velocity of an area wave propagating along the column which it calculates to be

$$u = \frac{c_s c_{Ai}}{\sqrt{c_s^2 + c_{Ai}^2}} = c_s(1-\beta)^{1/2} \qquad \text{for} \quad \gamma = 2. \tag{29}$$

This goes to zero for $\beta = 1$. Here $c_s = \sqrt{\gamma p_i/\rho_i}$ and $c_{Ai} = \sqrt{B_i^2/4\pi\rho_i}$ are respectively the internal sound speed and Alfven velocity; β is defined as the ratio of the internal plasma pressure to the total external pressure. However, our simulation results for $\beta = 1$ show a finite velocity for the area wave which satisfies the relation

$$u = \frac{c_s\sqrt{c_{Ai}^2 + c_{Ae}^2 ak}}{\sqrt{c_s^2 + c_{Ai}^2 + c_{Ae}^2 ak}} \qquad \text{with} \quad c_{Ae}^2 = \frac{B_e^2}{4\pi\rho_i}, \tag{30}$$

where a is half of the column width and k is the axial wavenumber. Using the smallest value of k which fits in the column ($k = 2\pi/L$) and the flow out speed, the confinement time is finite and agrees with our observations. Equation (30) is obtained analytically by including the tension effect due to the magnetic field curvature being nonzero at $\beta = 1$; the previous theories neglected this effect. The density contours and the field intensity contours are shown in Fig. 4, where one can see a rarefraction wave propagating toward the center. It is clear that the tension of the magnetic field lines open the throat while the low plasma pressure leads to a narrow channel. This tendency to stay open is responsible for the finite confinement time at $\beta = 1$ [20]. A similar confinement time as well as similar wave pattern have been reported by Brackbill [21] using a different but quite sophisticated and complex MHD algorithm. This lends again to confidence in the present algorithm for its accuracy and versatility. Anisotropic presure effects could be included in the model and would probably lead to improved predictions on confinement.

(C) *Global Simulations of the Magnetosphere*

The first self-consistent MHD simulations of a supersonic plasma flow, modeling the solar wind, impinging upon a dipole field, representing the earth's magnetic field, were carried out [15, 22, 23] using the Lax version of our particle MHD code [3]. Three dimensional Lax simulations have also been successfully carried out [24].

Because of the large numerical diffusion inherent to the Lax scheme, magnetic Reynolds numbers of order only 3–10 were obtained and a very short unrealistic magnetosphere tail resulted. However, with the Lax–Wendroff scheme, numerical resistivity is much smaller and more realistic simulations at higher magnetic Reynolds number can now be performed by appropriately introducing a variable resistivity in the algorithm. We present here two simulations of the magnetosphere: one resistive with the Lax scheme and the other for the same parameters but with the Lax–Wendroff scheme at higher Reynolds number.

A 2–1/2 dimension NGP version of the MHD particle code as described in Section III with 32×16 unit grids and four particles per cell is used. The dipole field of the earth is generated by two closely spaced current filaments of equal magnitude but opposite sign out of the simulation plane. At $t = 0$, all particles are uniformly distributed and given a uniform flow velocity v_f in the x direction such that $v_f = 2c_s$, where c_s is the speed of sound. This solar wind carries its own magnetic field which is pointing to the negative y-direction (southward) and is of strength such that $c_A = 0.2\, c_s$. Periodic boundary conditions are imposed on the magnetic field while

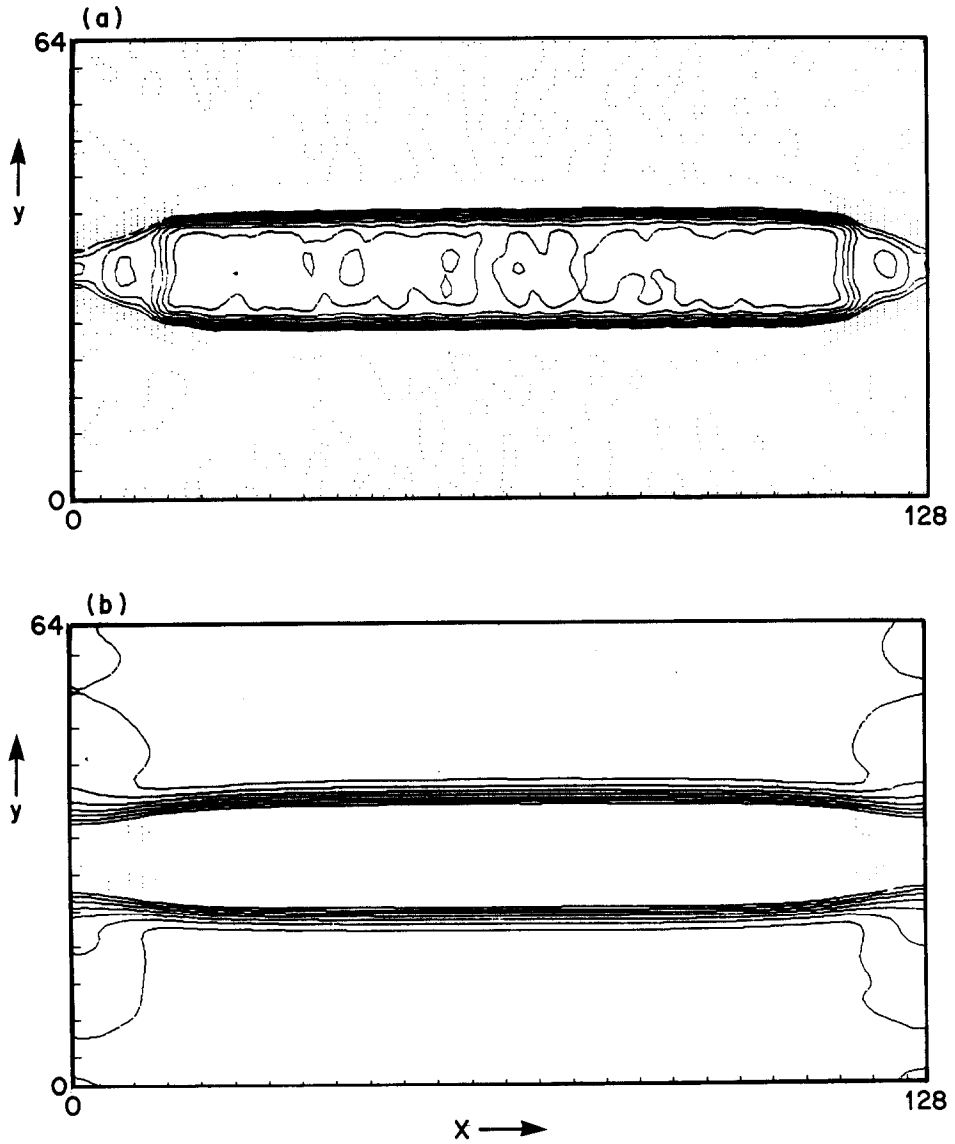

FIG. 4. Plasma column endloss; (a) density contours at $t = 20\Delta/c_s$, where one can see a rarefraction wave propagating toward the center, (b) the contours of B_x intensity show that the throat does not close on the density contours due to curvature tension.

particles which leave the system at the edges are reintroduced as fresh particles in the first x-cell with their original flow velocity and random position along the y-axis. In this way, t incoming flow is relatively independent of the presence of the obstacle; however some magnetic disturbance is introduced into the solar wind.

The Lax scheme used to update the magnetic field through the finite difference induction equation introduces a numerical resisitivity which is given by [25]

$$\eta = (\Delta^2/2N\Delta t - \Delta t c^2/2). \tag{31}$$

The quantities Δ, N, Δt, and c are respectively the unit grid spacing, the dimensionality (here $N = 2$), the time step and some characteristic maximum signal speed on the mesh. The first term comes from the lack of time centering and the second from the spatial averaging of the field over neighboring grid points as required by stability. For the problem investigated with the Lax scheme, the time step is chosen such that $\Delta t < 1/\sqrt{2}\, c$ and the first term in Eq. (31) dominates. The magnetic Reynolds number $R_m = lv/\eta$ is then written as $R_m \simeq lv(2N\Delta t)/\Delta^2$. For the example in point, $v = v_f$, $\Delta t = 0.1$, $\Delta = 1$ and $N = 2$, so that $R_m \sim 0.8l$, where l is taken as the characteristic length of variation of the dipole field and is such that $5\Delta \lesssim l \lesssim 10\Delta$, which means that $R_m \sim 4$–8.

The magnetic field topology obtained with the Lax scheme is displayed in Fig. 5a). Contours of the z-component of the vector potential depict the field lines at time $t = 5c_s^{-1}\Delta$. The classic Dungey pattern of the reconnected magnetosphere is obtained with x-points at the nose and tail where southward solar wind field and dipole field merge. This happens close to the vacuum superposition points and there is about the same distance between nose and tail x-points and the dipole center. This is because of our low magnetic Reynolds number and diffusion dominates over convection.

A run on the Lax–Wendroff code is unstable without explicitly imposed ("physical") resistivity, because there is no dissipation to allow the fluid to shock and no possibility for the solar wind field to reconnect. We note a pile-up of the flows in front of the dipole and numerical instability results. Addition of some resistivity stabilizes the code. Following Ref. [7], we introduce finite resistivity in the second step of the Lax–Wendroff algorithm by a four point angled derivative and the field pushing equation in finite difference form becomes

$$\begin{aligned} \boldsymbol{B}^{n+1} = \mathbf{B}^n &+ \Delta t[\boldsymbol{\Delta} \times (\mathbf{v} \times \mathbf{B})]^{n+1/2} \\ &+ \frac{\Delta t}{2\Delta^2}\eta[\mathbf{B}_{i+1,j+1} + \mathbf{B}_{i-1,j-1} + \mathbf{B}_{i+1,j+1} \\ &+ \mathbf{B}_{i-1,j-1} - 4\mathbf{B}_{i,j}]^n, \end{aligned} \tag{32}$$

where the superscript n refers to the time step, i.e., $t = n\Delta t$, and the subscripts i and j indicate the grid points in the x- and y-directions. This algorithm performs well for constant η and requires that $\Delta t < \Delta^2/\eta$.

For large values of η and the same parameters, we recover the Lax results of Fig. 5a). For $\eta = 0.5$, a Reynolds number $R_m \sim 4l$ or $R_m \sim 20$–40 is obtained. The magnetic field lines for this case are presented in Fig. 5b) at time $t = 5c_s^{-1}\Delta$.

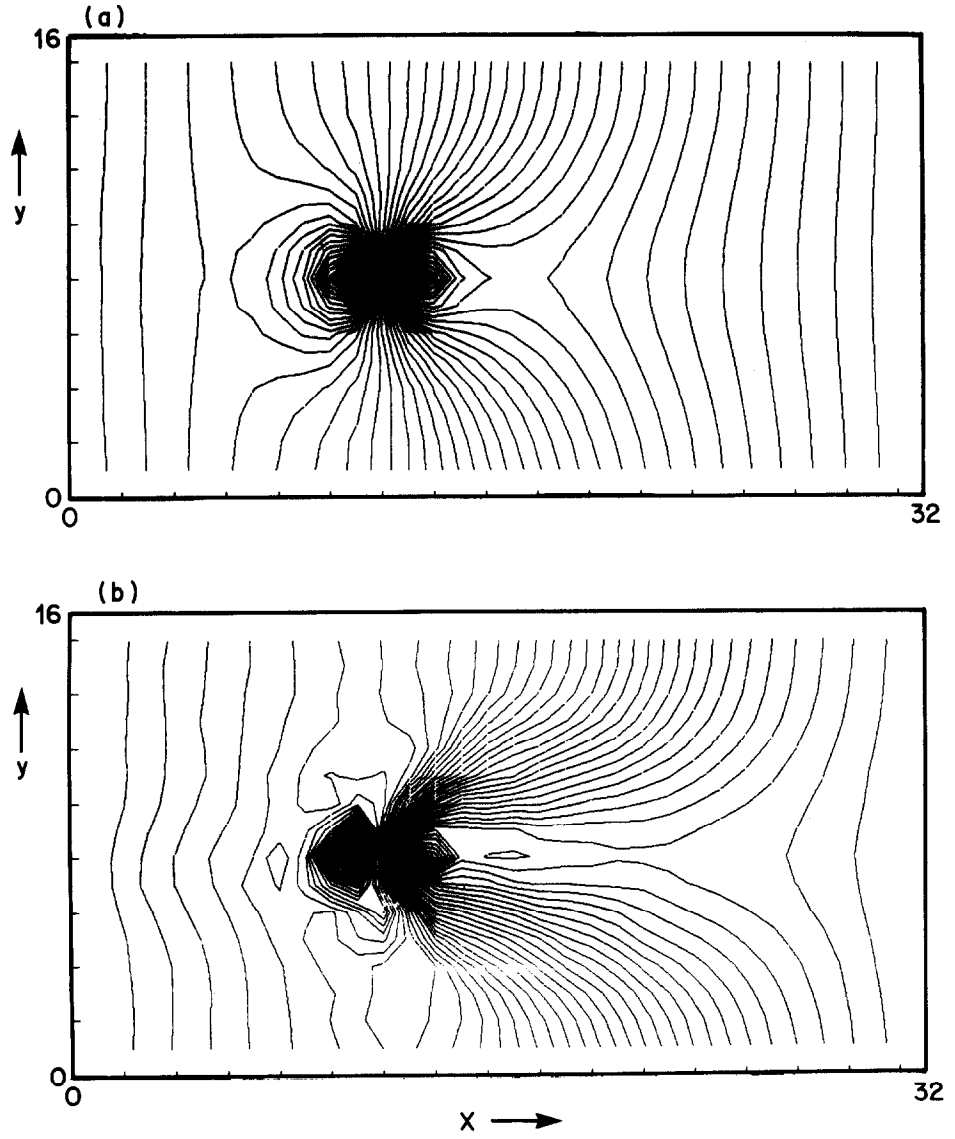

FIG. 5. Magnetic field lines for the magnetosphere computed with (a) Lax scheme and (b) Lax–Wendroff scheme; a much longer tail is seen due to the lesser magnetic diffusion.

Convection dominates over diffusion and the tail is now stretched out substantially, a feature believed to be naturally occurring. Reconnection at the nose also takes place, but is somewhat obscured by the reentry of the now longer tail magnetic field in front of the dipole.

VI. Summary and Conclusions

Marked improvements in the MHD particle code [1] have been achieved on two fronts: one by improving the particle quantity assignments to grid points and grid quantity assignments to particles and the other by implementing the Lax–Wendroff algorithm for magnetic field advancement. For the first of these, various versions of assignment have been tried and compared. The most successful among them are the subtracted dipole interpolation assignment in the code where differentiation operations are handled in Fourier space and the area weighting assignment using a two grid system in a code where finite differencing is employed. These two versions have some pluses and minuses on different aspects of code qualities when compared with each other; both of these, when compared with the nearest grid point assignment, show much improved properties. For the second aspect, implementation [illegible] diffusion terms are required for numerical stability, the straightforward implementation (Table I) of this algorithm for the magnetic induction equation suffices without any artifical terms.

The properties of the present code and its versatility as well as its resilience have been demonstrated in extensive standard tests of wave propagation using temporal autocorrelation functions and in a number of other physical applications. In these applications the present code has yielded reasonable physics results where the earliest version of the code was unable to do so. Examples in point are investigations of the ballooning instability, investigations of the high-beta column outflow problem and the elimination of highly resistive results in the magnetosphere flow problem.

Acknowledgments

This work was supported by the National Science Foundation Contracts Number PHY 79-01319 and ATM 79-26492 and the United States Department of Energy Grant AM03-76500010 PA 26, Task III.

References

1. R. L. Morse, *in* "Method of Computational Physics" (B. Alder *et al. Eds.*), Vol. 9, p. 213, Academic Press, New York, 1970.
2. B. M. Marder, *Math. Comp.* **29** (1975), 434.
3. J. N. Leboeuf, T. Tajima, and J. M. Dawson, *J. Comput. Phys.* **31** (1979), 379.
4. K. Mima, T. Tajima, and J. N. Leboeuf, *Phys. Rev. Lett.* **41** (1978), 1715.
5. T. Tajima, J. N. Leboeuf, and J. M. Dawson, *J. Comput. Phys.* **38** (1980), 237.
6. J. P. Boris and D. L. Book, *J. Comput. Phys.* **11** (1973), 38.
7. D. E. Potter, "Computational Physics," Academic Press, New York, 1973.
8. W. L. Kruer, J. M. Dawson, and B. Rosen, *J. Comput. Phys.* **13** (1973), 144.
9. J. P. Boris and D. L. Book, *J. Comput. Phys.* **20** (1976), 397.
10. R. D. Richtmyer and K. W. Morton, "Difference Methods for Initial Value Problem," Wiley–Interscience, New York, 1967.

11. A. B. LANGDON, *J. Comput. Phys.* **6** (1970), 297.
12. T. TAJIMA, F. BRUNEL, J. N. LEBOEUF, AND J. M. DAWSON *in* "Proceedings of the Ninth Conference on Numerical Simulation of Plasmas," p. 0A-5, Northwestern University, Department of Mechanical and Nuclear Engineering, Evanston, Illinois, June 30–July 2, 1980.
13. W. L. KRUER, *Nucl. Tech.* **27** (1975), 216.
14. A. B. LANGDON, *Phys. Fluids* **22** (1979), 163.
15. J. N. LEBOEUF, T. TAJIMA, C. F. KENNEL, AND J. M. DAWSON, *in* "Computational Modeling of Magnetospheric Processes" (W. O. Olson, Ed.), Geophysical Monograph No. 21, p. 536, AGU, Washington, D.C., 1979.
16. I. B. BERNSTEIN, E. A. FRIEMAN, M. D. KRUSKAL, AND R. M. KULSRUD, *Proc. Royal Soc. A* 244 (1958), 17.
17. A. H. GLASSER, *in* "Proceedings of the Finite Beta Theory Workshop, Varenna, Italy" (B. Coppi and W. Sadowski, Eds.), U.S. DOE-CONF 7709167, 1977.
18. The particle MHD code (as is) cannot naturally handle a global vacuum and the code has not yet been developed to treat matching to plasma–vacuum interfaces. The particle MHD code is, however, stable if the region of zero density only covers a few cells. The code with localized vacuum still satisfies in a global sense the CFL condition (itself defined in a global way: the Alfven wave is not localized at one grid point.)
19. J. B. TAYLOR AND J. A. WESSON, **5** (1965), 159.
20. F. BRUNEL, T. TAJIMA, J. N. LEBOEUF, AND J. M. DAWSON, *Phys. Rev. Lett* **44** (1980), 1494.
21. J. U. BRACKBILL, M. T. MENTZEL, AND D. C. BARNES, *in* "Topical Conference on Pulsed High Beta Plasma," (D. E. Evan, Ed.), p. 345, Pergamon, New York, 1976.
22. J. N. LEBOEUF, T. TAJIMA, C. F. KENNEL, AND J. M. DAWSON, *Geophys. Rev. Lett.* **5** (1978), 609.
23. T. TAJIMA, *Bull. Amer. Phys. Soc.* **23** (1978), 762.
24. J. N. LEBOEUF, T. TAJIMA, C. F. KENNEL, AND J. M. DAWSON, *Geophys. Rev. Lett.* **8** (1981), 257.
25. K. V. ROBERTS AND D. E. POTTER, *in* "Methods in Computational Physics" (B. Alder *et al.*, Eds.), Vol. 9, p. 339, Academic Press, New York, 1970.